| **Titre:**<br>Title: | Manufacturing composite beams reinforced with three-dimensionally patterned-oriented carbon nanotubes through microfluidic infiltration |
|---|---|
| **Auteurs:**<br>Authors: | Rouhollah Dermanaki Farahani, Maryam Pahlavanpour, Hamid Dalir, Brahim Aïssa, My Ali El Khakani, Martin Lévesque, & Daniel Therriault |
| **Date:** | 2012 |
| **Type:** | Article de revue / Article |
| **Référence:**<br>Citation: | Farahani, R. D., Pahlavanpour, M., Dalir, H., Aïssa, B., Khakani, M. A. E., Lévesque, M., & Therriault, D. (2012). Manufacturing composite beams reinforced with three-dimensionally patterned-oriented carbon nanotubes through microfluidic infiltration. Materials & Design, 41, 214-225. https://doi.org/10.1016/j.matdes.2012.05.005 |

## Document en libre accès dans PolyPublie
Open Access document in PolyPublie

| **URL de PolyPublie:**<br>PolyPublie URL: | https://publications.polymtl.ca/10398/ |
|---|---|
| **Version:** | Version finale avant publication / Accepted version<br>Révisé par les pairs / Refereed |
| **Conditions d'utilisation:**<br>Terms of Use: | CC BY-NC-ND |

## Document publié chez l'éditeur officiel
Document issued by the official publisher

| **Titre de la revue:**<br>Journal Title: | Materials & Design (vol. 41) |
|---|---|
| **Maison d'édition:**<br>Publisher: | Elsevier |
| **URL officiel:**<br>Official URL: | https://doi.org/10.1016/j.matdes.2012.05.005 |
| **Mention légale:**<br>Legal notice: | © 2012. This is the author's version of an article that appeared in Materials & Design (vol. 41) . The final published version is available at https://doi.org/10.1016/j.matdes.2012.05.005. This manuscript version is made available under the CC-BY-NC-ND 4.0 license https://creativecommons.org/licenses/by-nc-nd/4.0/ |

# Manufacturing composite beams reinforced with three-dimensionally patterned-oriented carbon nanotubes through microfluidic infiltration

Rouhollah D. Farahani[a], Maryam Pahlavanpour[a], Hamid Dalir[a], Brahim Aissa[a], My Ali El Khakani[b], Martin Lévesque[a], Daniel Therriault[a]*

[a] Center for Applied Research on Polymers and Composites (CREPEC), Mechanical Engineering Department, École Polytechnique de Montréal, C.P. 6079, Succ.Centre-Ville, Montreal (QC), Canada H3C 3A7

[b] Institut National de la Recherche Scientifique, INRS-Énergie, Matériaux et Télécommunications, 1650 Blvd.Lionel-Boulet, Varennes (QC), Canada J3X 1S2

* Corresponding author:

Phone: 1-514-340-4711 x4419

Fax: 1-514-340-4176

E-mail: daniel.therriault@polymtl.ca

## Abstract

Functionalized single-walled carbon nanotubes (SWCNTs)/epoxy nanocomposite suspensions were prepared and injected into three-dimensional (3D) interconnected microfluidic networks in order to fabricate composite beams reinforced with patterned oriented nanotubes. The microfluidic networks were fabricated by the robotized direct deposition of fugitive ink filaments in layer-by-layer sequence onto substrates, followed by their epoxy encapsulation and the ink removal. Then, the nanocomposite suspensions prepared by ultrasonication and three-roll mill mixing methods were injected into the empty networks under two different controlled and constant pressures in order to subject the suspensions to different shear conditions in the microchannels. Morphological studies

1

revealed that the SWCNTs were preferentially aligned in the microchannels along the flow direction at the higher injection pressure. The improvement of Young's modulus of the manufactured 3D-reinforced rectangular beams prepared at the high injection pressure was almost doubled when compared to that of beams prepared at the low injection pressure. Finally, the stiffness of the 3D-reinforced beams was compared with the theoretically predicted values obtained from micromechanical model. The analytical predictions give a close estimation of the stiffness at different micro-injection conditions. Based on the experimental and theoretical results, the present manufacturing techniques enable the spatial orientation of nanotube in the final product by taking advantage of shear flow combined with dimensional constraining inside the microfluidic channels.

Keywords: Nanocomposites, Nanotube orientation, Analytical modeling

1. Introduction

   Single-walled carbon nanotubes (SWCNTs) reinforced polymer nanocomposites have attracted considerable attention for a wide variety of applications such as high-performance polymer composites [1], actuators and sensors [2], shape memory polymers [3], electrostatic microvalves [4] and communication systems [5]. Production of high quality carbon nanotubes (CNTs) having large aspect ratio, their proper dispersion and orientation in polymer matrices as well as the improvement of interfacial bonding are the main parameters affecting nanocomposite mechanical performance [6]. Grafting chemical groups to the surface of CNTs is the usual approach to minimize nanotubes agglomeration and also to enhance their interfacial interactions with the polymer matrix [7-9]. Carboxylic groups grafted during the acid purification process of the CNTs [10] as well as the non-covalent functionalization using surfactants like porphyrin [11], can significantly improve interfacial stress transfer [12,13].
   To address the CNTs alignment along a desired direction in polymer matrix, shear flow [14,15] and electromagnetic field [16] along with dimensional constraints have been used. The injection of nanocomposites under high shear flow causes CNTs to be aligned

2

in the direction of the flow where the degree of orientation directly depends on the extent of applied shear [14,15]. However, depending on the type of flow, most of the nanotubes remain randomly oriented and shear-induced orientation of CNTs takes place only at high shear zones. Dimensional constraining effect on CNTs orientation in 1D and 2D has been employed in several nanocomposite processing techniques including fiber spinning and electrospinning [17], compression molding [16], extrusion [18] and film casting [19]. None of these techniques enable manufacturing a final product with sufficient control on the threedimensional (3D) orientation of the reinforcement. More recently, an approach based on the micro-infiltration of microfluidic networks with nanocomposite suspensions has been developed to manufacture 3D-reinforced microstructure beams [20]. This approach typically attempts to design optimized microstructures using different thermosetting matrices and nanofillers. However, these studies have not addressed the influence of manufacturing process conditions such as channels diameter, injection pressures or shear rates on CNTs orientation and its resulting influence on the mechanical properties of 3D reinforced beams.

In this paper, 3D-reinforced microstructure beams were manufactured via micro injection of 3D microfluidic networks with purified SWCNTs/epoxy nanocomposite suspension at different injection pressures. After curing the nanocomposite suspension, the final product was a rectangular beam reinforced with a complex 3D nanocomposite microfiber scaffold. The main goal is the fabrication of nanocomposite beams reinforced with threedimensionally oriented SWCNTs by taking the advantages of high shear flow and also dimensional constraining in small diameter interconnected microfluidic channels. In addition to dimensional constraining, the microchannels present large shear surfaces, involved in the shear-induced orientation of CNTs. The effective process related apparent shear rates inside the microfluidic channels in micro injection process were estimated from capillary viscometry. The morphology of the nanocomposite and 3D reinforced beams were characterized under scanning electron microscopy (SEM), transmission electron microscopy (TEM) and their mechanical properties were measured under tensile testing. Furthermore, a micromechanical model is used to predict the effective stiffness of the manufactured 3D reinforced beams in order to estimate if the manufactured samples

3

reached their full potential. Our results provide sufficient evidence for the effectiveness of the present manufacturing approach to enhance the stiffness of the nanocomposites caused by homogenously aligning CNTs throughout the final product.

## 2. Experimental

### 2.1. Materials

The SWCNTs were produced by means of the pulsed laser ablation technique, using an excimer KrF laser (248 nm, 20 ns, 50 Hz, 300 mJ) with a graphite target and Co/Ni F D W D O \ V W   L Q   D   I X U Q D F H   D W   [21]. The as-produced SWCNTs n   D W P R V S K were chemically purified and functionalized by refluxing them in a $3N$ $HNO_3$ (Sigma-Aldrich) solution for 5 h (more details on the SWCNTs purification can be found elsewhere [10]). Zinc Protoporphyrin IX (ZnPP) obtained from Sigma Aldrich was used as the surfactant. The two epoxy systems used in this study were a special one-component dual cure (ultraviolet/heat curable) epoxy resin (UV-epoxy, UV15DC80, Master Bond Inc.) and a two-component epoxy system composed of EPON resin 862 (Miller-Stephenson Chemical Company, Inc.) and ANCAMINE 2049 (Air Products Inc.) as the hardener. The UV-epoxy used here contains a UV photo-initiator having an optimal absorption at 365 nm and a heat initiator active in the 60–80°C range.

### 2.2. Preparation of nanocomposites

The nanocomposites were prepared by blending the UV-epoxy and purified SWCNTs at two loads of 0.5wt% and 1wt%. The desired amount of purified SWCNTs was added to a solution of 0.1 mM of zinc protoporphyrin IX in acetone (Sigma-Aldrich). The suspension was sonicated in an ultrasonic bath (Ultrasonic cleaner 8891, Cole-Parmer) for 30 min. The UV-epoxy was then slowly mixed with the nanotube suspension in acetone over a magnetic stirring hot plate (Model SP131825, Barnstead international) at 50°C for 4 h. After stirring, the nanocomposite mixture was simultaneously sonicated and heated in the ultrasonication bath at 50°C for 1 h. The residual trace of solvent was evaporated by heating the nanocomposite mixture at 30°C for 12 h and at 50°C for 24 h in a vacuumed-oven (Cole

4

Parmer). After the evaporation of the solvent, the nanocomposites were passed through a three roll mill mixer (Exakt 80E, Exakt Technologies) for final high shear mixing. The gaps between the rolls varied in three batch-wise processing steps including 5 passes at 25 μm, 5 passes at 10 μm and 10 passes at 5 μm, respectively. The speed of the roll was set to 250 RPM. The final mixture was then degassed under vacuum for 24 h.

### 2.3. Micro-injection of 3D microfluidic networks

Three dimensional microscaffolds were fabricated using a computer-controlled robot (I & J 2200-4, I & J Fisnar) that moves a dispensing apparatus (HP-7X, EFD) along the x, y and z axes [22,23]. The fabrication of the microscaffold began with the deposition of the ink-based filaments on an epoxy substrate, leading to a two-dimensional pattern. The fugitive ink was a 40 wt% binary mixture of a microcrystalline wax (SP18, Strahl & Pitstch) and a petroleum jelly (Lever Pond's). The following layers were deposited by successively incrementing the z-position of the dispensing nozzle by the diameter of the filaments. The 3D microscaffold consisted of eleven layers of fugitive ink filaments, deposited alternatively along and perpendicular to the scaffold longitudinal axis. The filament diameter was 150 μm for a deposition speed of 4.7 mm/s at an extrusion pressure of 1.9 MPa. The overall dimensions of the 3D ink structure were 62 mm in length, 8 mm in width and 1.7 mm in thickness with 0.25 mm spacing between filaments. The empty space between the scaffold filaments was filled with the same epoxy resin used for the substrate fabrication. Upon the curing of the epoxy, the fugitive ink was removed from the structure by the liquefaction at 100°C and applying vacuum, yielding an interconnected 3D microfluidic network. Figure 1a shows a schematic of a typical rectangular beam which consists of a microfluidic network embedded in the epoxy resin with its overall dimens.

The created tubular microfluidic network was filled by nanocomposite suspension, through a plastic tube attached to the opened channels using the fluid dispenser as shown in Figure 1b. The micro-injection processed to the fabrication of 3D reinforced nanocomposite rectangular beam (i.e., nanocomposite-injected beams). The injection pressure was set either to 0.7 MPa (defined as low injection pressure) or 4.2 MPa (defined
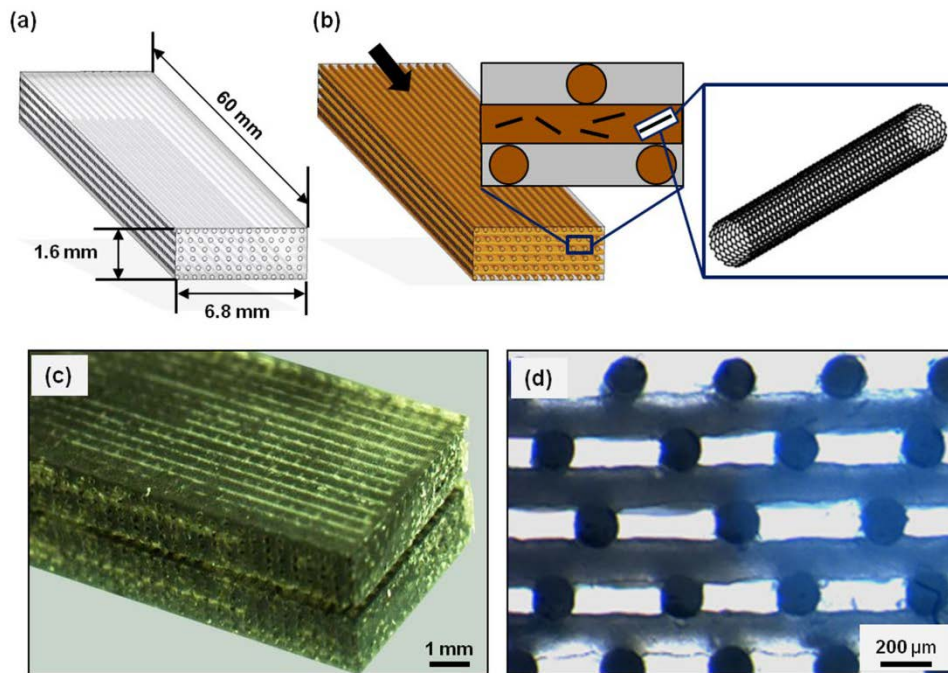
5

Figure 1. Illustration of the manufacturing process of a 3D beam reinforced with real and localized SWCNTs through micro-injection of 3D microfluidic network: (a) overall dimensions of the microfluidic network beams, fabricated by the direct-writing of the fugitive ink upon epoxy encapsulation and ink removal, (b) micro-injection of the empty network with nanocomposite suspension which lead to fabrication of 3D reinforced beams (the arrow shows the direction of injection flow), (c) isometric image of a 3D reinforced beam, (d) typical cross-section of a nanocomposite injected beam, showing the configuration of microchannels filled with nanocomposites.

ashigh injection pressure). For comparison purposes, beams filled with pure UV-epoxy (defined as resin-injected beams) were also prepared. Shortly after the injection, the beams filled by the UV-epoxy- and its nanocomposites were put under illumination of a UV lamp (RK-97600-00, Cole-Parmer) for 30 min for pre-curing in order to avoid effect of Brownian motion on the CNTs orientation. Resin- and nanocomposite (NC)-injected beams were then post-cured in the oven at 80 °C for 1 h followed by 130°C for another 1 h. The beams were cut and polished to the desired dimensions (i.e., ~60 mm in length, ~6.8 mm in width and ~1.6 mm in thickness) for mechanical and morphological characterizations. Figure 1c shows an isometric view of a NC-injected beam, prepared by the nanocomposite suspension with the nanotube load of 0.5wt% and Figure 1d shows the cross-section of the beam (microscale).

6

## 2.4. Nanotube and nanocomposites morphological characterizations

The purified SWCNTs were observed by transmission electron microscopy (TEM) using a Jeol JEM2100F (FEG-TEM, 200 kV) microscope. The nanotubes Raman spectra were acquired at room temperature in the 100 - 2000 cm⁻¹ spectral region under ambient conditions using a back-scattering geometry on a micro-Raman spectrometer (Renishaw Imaging Microscope Wire TM) with a 50× objective to focus the laser beam on the samples. Sample excitation was performed using a 514.5 nm (2.41 eV) line from an air cooled Ar+ laser. In addition, the SWCNTs were characterized by X-ray photoelectron spectroscopy (XPS, Escalab 220i-XL system, VG instruments) using the monochromatic Al Kα radiation as the excitation source (1486.6 eV, full width half-maximum of the Ag 3d5/2 line = 1 eV at 20 eV pass energy). Fracture surface of the 3D-reinforced and the bulk nanocomposite beams were observed using field emission scanning electron microscopy (FESEM, JEOL, JSM-7600TFE) at 2 kV in order to observe the failure modes. The orientation state of the CNTs in the NC-injected beams was studied under TEM (JEOL, JEM2100F). Prior to observation, the samples were prepared by ultramicrotoming of the NC-injected beams surfaces using a diamond knife at room temperature.

## 2.5. Viscosity characterization

Since the degree of CNTs orientation depends on the shear rate (or applied injection pressure) of nanocomposite flow, the shear conditions through the micro-injection of 3D microfluidic networks were studied at the two different injection pressures. The complexity of the nanocomposite flow pattern inside the complex 3D interconnected microfluidic network prevents accurate shear conditions to be characterized. Since the accurate modeling of the nanocomposite flow is not the main focus of this study, a simple assumption was made to estimate the process-related shear rates encountered in the micro-injection process. The microfluidic network was assumed as a bundle of similar disconnected parallel channels in which the flow pattern is corresponding to a simple Poiseuille flow. This flow mechanism may also occur in pressure-constant capillary viscometry. Therefore, the process-related apparent shear rate and apparent viscosity of the

pure UV-epoxy and its nanocomposites in the microfluidic network were estimated from an experimental method based on capillary viscometry [10, 24]. For the purpose of similarity (i.e., similar flow conditions in micro-injection process and capillary viscometry), the materials were extruded through a micro-nozzle (5132-0.25 Precision Stainless Steel Tips, EFD, L = ~20 mm and D = 100 μm) under the same applied pressures used for the micro-injection of empty microchannels with nanocomposites (i.e., 0.7 MPa and 4.2 MPa). To obtain the materials flow rate, ten continuous filaments of materials were deposited over a glass substrate using the computer-controlled robot and the fluid dispenser. Shortly after the deposition, the filaments were cured under illumination of the UV lamp for 5 min. The flow rates of the materials were calculated from the cross section of the filaments and the deposition speed controlled by dispensing apparatus. The cross section area of the filaments was measured using an optical microscope (BX-61, Olympus) and image analysis software (ImagePro Plus v5, Media Cybernetics). The process-related apparent shear rate and the process-related apparent viscosity were calculated based on capillary viscometry equations including Rabinowitsch correction [24].

## 2.6. Mechanical properties

Mechanical properties (i.e., tensile modulus, strength and elongation at break) of the beams were measured in tensile testing machine (Instron 4400R) with a load cell of 5 kN according to the ASTM D638 standard. The crosshead speed was set to 1 mm/min and typical dimensions of the sample beams were 6 mm × 6.8 mm × 16 mm.

## 3. Mechanical modeling

A three-step analytical homogenization procedure was developed to estimate the resin- or NC-injected beams effective mechanical properties (Figure 2). The first homogenization step was used to estimate the mechanical properties of NC fibers. The mechanical properties of the beams layers were calculated in the second homogenization step. The third step was used to derive the injected beams effective properties. The different phases (i.e., the epoxy matrix in the microfibers, the EPON
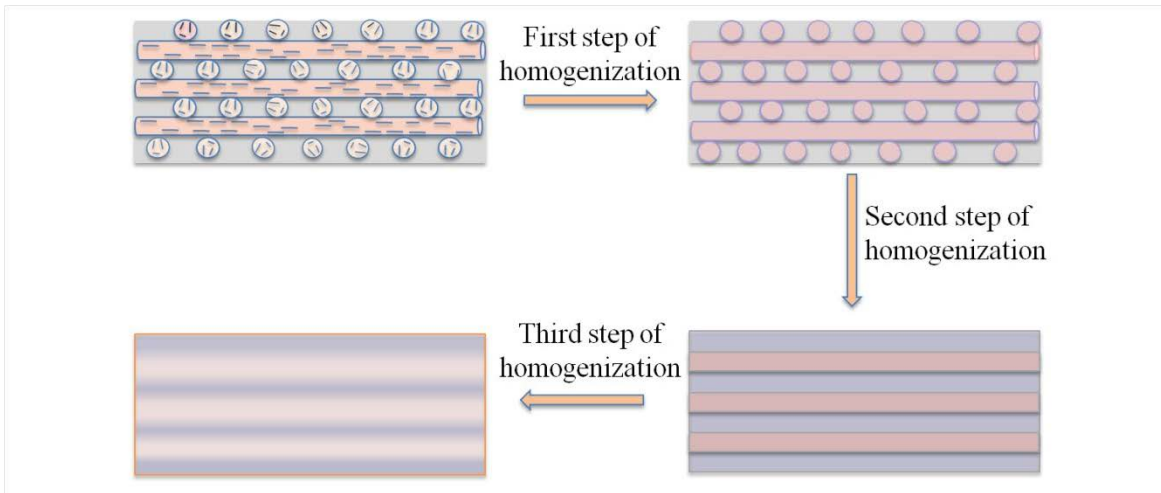
8

Figure 2 Schematic of homogenization steps

862 matrix around the microfibers and the carbon nanotubes) assumed to be linearly elastic and perfectly bonded. The Mori-Tanaka method [25] was used in the first and second homogenization steps while the Classical Lamination Theory was used at the last step According to the Mori-Tanaka scheme, the effective stiffness tensor, $C_{MT}$, for a two-phase material is given by:

$$C_{MT} = C_m + c_i[(C_i - C_m):T][(1-c_i)I + c_iT]^{-1}, \qquad (1)$$

where $C_m$ and $C_i$ refer respectively to matrix and reinforcement stiffness tensors and $c_i$ is the reinforcement volume fraction. $T$ is given by:

$$T = [I + S:C_m^{-1}:(C_i - C_m)]^{-1}, \qquad (2)$$

where $S$ is the fourth-order Eshelby's tensor [26] that depends on the reinforcement shape as well as the matrix properties (the detailed expression for Eshelby's tensor can be found in Appendix A).

Equation (1) leads to a transversely isotropic material if it is applied to a composite reinforced by aligned carbon nanotubes.
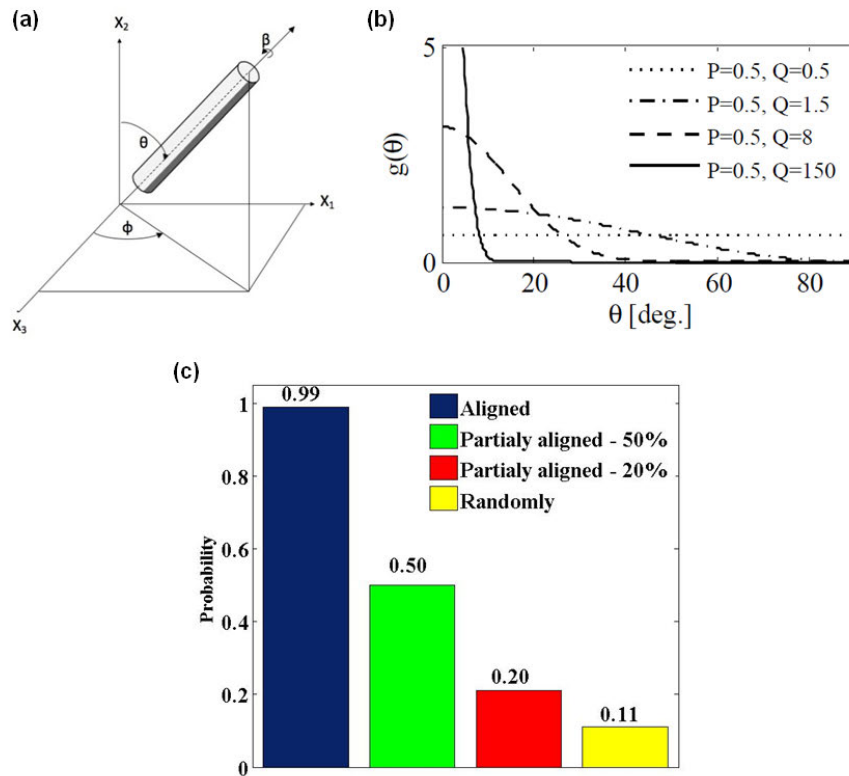
9

Figure 3. (a) Euler angles, (b) Orientation Probability Density Function (OPDF) and (c) probability of finding a CNT oriented at $\mp 10^q$ from $x_2$.

When nanotubes are oriented arbitrarily, a weighted orientation averaging must be used to obtain the effective elasticity tensor $\langle C \rangle$, as:

$$\langle C \rangle = \frac{\int_0^{2S}\int_0^{S}\int_0^{2S} g\left(T, M, E\right) C^{Tr}\left(T, M, E\right)\sin M\, dM\, dT\, dE}{\int_0^{2S}\int_0^{S}\int_0^{2S} g\left(T, M, E\right)\sin M\, dM\, dT\, dE}, \qquad (3)$$

where $g\left(T, M, E\right)$ is the Orientation Probability Density Function (OPDF) [27] and

$$C^{Tr}\left(T, M, E\right) = T\left(T, M, E\right) C_{MT} R\left(T, M, E\right)^{-1}, \qquad (4)$$

10

where $R$ and $R^T$ (details on $R$ can be found in [27]) are the corresponding rotation matrix and its transpose, $\gamma$, $\eta$ and $\xi$ as shown in Figure 3a are the Euler angles used for defining the CNT orientations. The OPDF can be interpreted as the probability of having a CNT oriented according to specific values of $\gamma$, $\eta$ and $\xi$. Note that $\sin(\eta)$ in equation (4) is due to the transformation to the spherical coordinate system. During the injection process, the shearing forces are symmetric with respect to the flow axis. As a result, it was assumed that the CNT orientation distribution was also axisymmetric with respect to the fiber axis $X_2$. Therefore, $g(\xi, \gamma, \eta)$ was simplified to $g(\eta)$ [27]. In this study, the OPDF introduced by Maekawa et al [28]

$$g(\eta) = \frac{(\sin \eta)^{2P-1}(\cos \eta)^{2Q-1}}{\int_0^{\frac{\pi}{2}} (\sin \eta)^{2P-1}(\cos \eta)^{2Q-1} d\eta}, \tag{5}$$

where $P$ and $Q$ are parameters accounting for the degree of reinforcement alignment, was used. Table 1 lists different values of $P$ and $Q$ and the corresponding orientations. Plots of OPDF for four different values of $P$ and $Q$ are illustrated in Figure 3b. Figure 3c shows the probability of finding a CNT oriented at $0^\circ$ from $X_2$.

Since nanotubes tend to form bundles, the elastic properties of SWCNT bundles reported in [29] were used as the reinforcement properties in the model:

$$C_{Nanotube} = \begin{pmatrix} 40.68 & 12.40 & 39.32 & 0 & 0 & 0 \\ 12.40 & 625.72 & 12.40 & 0 & 0 & 0 \\ 39.32 & 12.40 & 40.68 & 0 & 0 & 0 \\ 0 & 0 & 0 & 2.44 & 0 & 0 \\ 0 & 0 & 0 & 0 & 1.36 & 0 \\ 0 & 0 & 0 & 0 & 0 & 2.44 \end{pmatrix}. \tag{6}$$

11

Table 1. Values of P and Q and the corresponding orientations.

| Orientation | P | Q |
|---|---|---|
| Random | 0.5 | 0.5 |
| Partially aligned (20%) | 0.5 | 1.5 |
| Partially aligned (50%) | 0.5 | 8 |
| Aligned (99%) | 0.5 | 150 |

Equations (1) to (5) were used for the first homogenization step where $C_i$ was set to $C_{Nanotube}$. The UV-epoxy was assumed to be isotropic with a Young's modulus of 1.32 GPa and a Poisson's ratio of 0.3. Nanotube bundles aspect ratio was arbitrarily set to 200 and two different volume fractions (V. F.), 0.5 and 1% (equal to weight fraction since CNT and epoxy matrix have similar density) we considered.

For the second homogenization step, each layer was considered as a unidirectional ply (i.e. composites with completely aligned fibers). Equation (1) was used with $C_i$ equal to $\langle C \rangle$ obtained in the first step. The EPON 862 matrix was assumed to be isotropic with Young's modulus and Poisson's ratio of 3.1 GPa and 0.3, respectively. The aspect ratio of the fibers (the ratio of their length over their diameter) was set to 400 (i.e., long fibers).

The composite beam consists of two parts; longitudinal layers and transverse layers. The volume fraction of fibers in each layer was 34.67%, based on the number and dimension of fibers. Therefore, the beams stiffness tensor, $C_{Total}$, was obtained according to the Composite Laminate Theory as

$$C_{Total} = \frac{N_l C_l + N_t R_t C_t R_t^{T^*}}{N_l + N_t},$$ (7)

where l and t correspond to longitudinal and transverse directions, respectively. $C_l$ and $C_t$ were obtained from the second step and correspond to the $\langle C \rangle$ of the longitudinal and transverse layers, respectively. In this specific case, $C_l$ and $C_t$ were equal. N denotes the
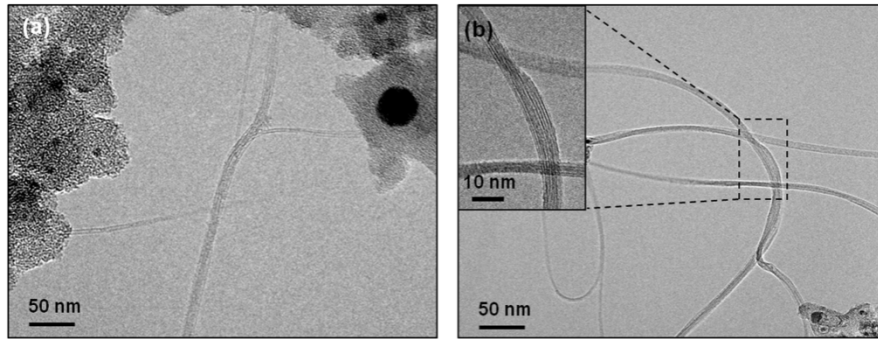
Figure 4. Typical TEM images of (a) the as-produced and (b) purified SWCNTs soot material

number of longitudinal and transverse layers that are 6 and 5, respectively. R is the rotation matrix corresponding to the 90° rotation of the transverse layers.

## 4. Results and discussion

### 4.1. Nanotube and nanocomposite morphological characterizations

Figure 4 shows typical TEM micrographs of the laser-synthesized SWCNTs before and after their chemical purification. The nanotubes are observed to self-organize most often into bundles, featuring a high aspect ratio since their length can reach up to several microns and their diameter is in the nanometer range. Figure 4a shows the TEM image of as-produced SWCNTs. In conjunction with the SWCNTs, other carbonaceous structures and impurities such as graphite and/or metal catalyst nanoparticles (dark in the TEM image) are observed. The nanotube chemical purification enabled to remove residual catalyst particles and other carbonaceous impurities as observed in Figure 4b.

Figure 5a shows typical Raman spectra of the as-produced and purified SWCNTs. The spectra represent three typical peaks for the nanotubes including a narrow radial breathing mode (RBM) band centered around 185, the D-band centered around 1350 $cm^{-1}$ and the G-band around 1600 $cm^{-1}$. The RBM band provides relevant information in terms of SWCNTs diameter [30]. Our SWCNTs are found to have a narrow diameter distribution centered around 1.2 nm. The G-band corresponds to the symmetric $E_{2g}$ vibrational tangential mode in graphite-like materials and the D-band is as a signature of disorder and/or defects in these structures. The G/D intensity ratio is generally used to
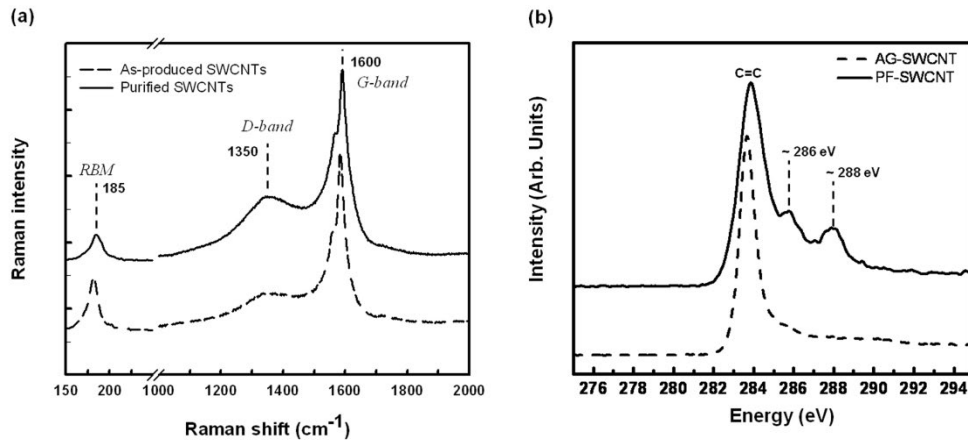
13

Figure 5. (a) Raman spectra and (b) photoelectron spectra of the nanotubes before and after chemical purification (acidic treatment)

assess the degree of purity of the nanotubes. After subjecting the nanotubes to the purification process, their G/D peak intensity ratio is seen to decrease significantly in comparison to that of the as-produced mats. This indicates that the nitric acid oxidization based purification process inherently creates additional structural defects in the nanotubes. This is also confirmed by the XPS analysis shown in Figure 5b. The XPS results that the C1s core level peak of purified SWCNTs is consisting of three clear components while that of as-produced samples exhibits only a relatively narrow C=C peak. The main peaks for both curves centered around 284.5 eV are due to the $sp^2$ bonding for the bulk structure of nanotubes. For the purified nanotubes, the two extra shoulders appearing clearly at ~ 286 eV and ~288 eV are attributed to C-O and/or C-NHx bonds, and to the COO group of carboxylic acid groups [31,32]. Based on the XPS results, the purification process has led to carboxylic groups grafting onto the SWCNTs surfaces (i.e., covalent functalization).

Figures 6a and 6b show the SEM images of the fracture surface of the bulk pure UV epoxy and its associated nanocomposite with the SWCNT loading of 0.5wt% respectively. The fracture surface of the pure epoxy resin is smooth while the nanocomposite shows a layered fracture surface. The larger roughness of the fracture surface of the nanocomposite sample might be attributed to possible toughening effect induced by the presence of carbon nanotubes as reported in literature [33]. Figures 6c and 6d show higher magnification images of their fracture surface. Based on Figure 6d, the absence of micro-size aggregates
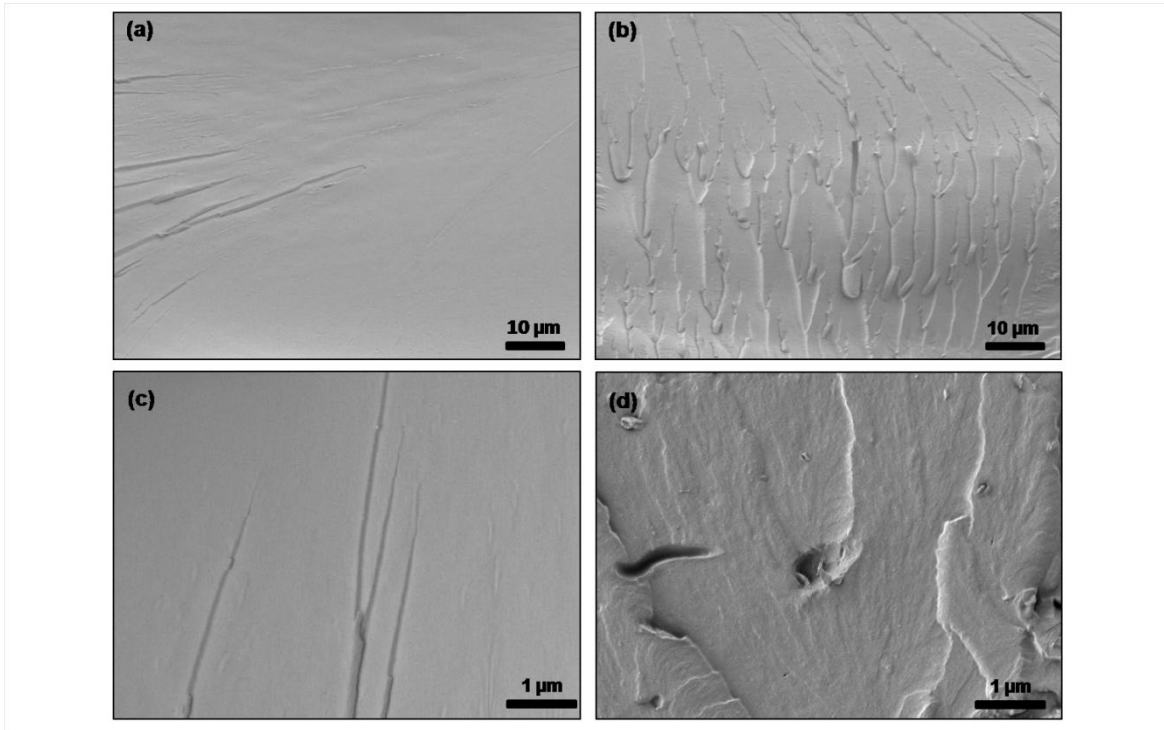
Figure 6. SEM images of the fracture surface of the bulk (a) epoxy and (b) its nanocomposite containing 0.5wt% purified SWCNTs after ultrasonication and three-roll mill mixing. (c) and (d) higher magnification images of (a) and (b), respectively.

of CNTs suggests a fairly uniform dispersion of the nanotube at least at the microscale. The surface modification of CNTs interface [34] and the effective mixing procedure including ultrasonication and three-roll mill mixing [11] are believed to be responsible for achieving the good dispersion of CNTs.

## 4.2. Shear rate estimation and viscosity characterization

Figure 7 shows the process-related apparent viscosity ($\eta_{app}$) with respect to the process-related apparent shear rate ($\dot{\gamma}_{app}$) induced by the extrusion of the pure UV-epoxy and its nanocomposites for five different extrusion pressures including two extrusion pressures corresponding to the low (shown as $P_1$) and high (shown as $P_2$) micro-injection pressures. The error bars are based on the standard deviations from the mean value obtained from the measurements. Although the estimation of shear conditions were needed only for
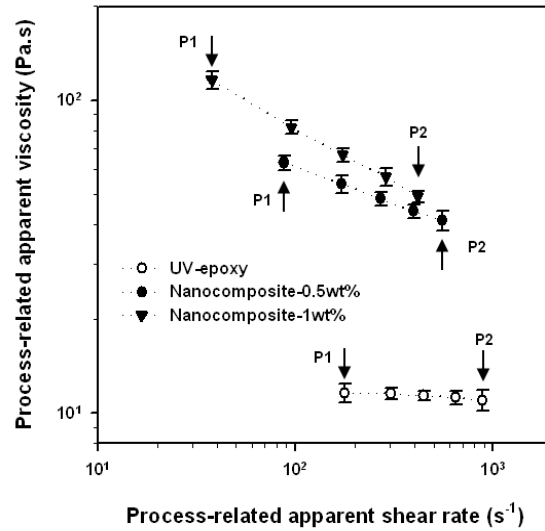
Figure 7. Viscosity-shear rate estimation of the pure UV-epoxy and its nanocomposites in microchannels using a method based on capillary viscometry.

two pressures (i.e., $P_1$ and $P_2$) corresponding to two micro-injection pressures, the viscosity-shear rate values were also obtained for the three additional pressures in order to study the rheological behavior of the materials for the pressures between $P_1$ and $P_2$. However, since the present viscometry is pressure-constant, different combinations of viscosity-shear rate were obtained for the neat epoxy and its nanocomposites for each extrusion pressure. Therefore, lower $\dot{\gamma}_{app}$ were obtained for the nanocomposites compared to the neat UV-epoxy at the same extrusion pressures due to the increase of viscosity with the addition of SWCNTs. Since the viscosity of nanocomposite is a good indicator of the quality of nanotube dispersion, the reasonable increase of the nanocomposite viscosity compared to the pure resin could support the effectiveness of nanocomposite mixing processes.

The incorporation of SWCNTs into the epoxy led to the apparition of shear-thinning behavior (i.e., negative slope, decrease of viscosity with increase of shear rate). This slight shear-thinning behavior might be attributed to the nanotubes orientation along the flow direction at higher shear rates. Table 2 lists the values estimated for $\eta_{app}$ and $\dot{\gamma}_{app}$ of the materials only for the two pressures (i.e., $P_1$ and $P_2$). According to capillary viscosity equations [24], applying higher pressure gradient will lead to higher shear rates. The open

16

Table 2. Estimation of the process-related apparent viscosity and the process-related apparent shear rate in microfluidic network.

| Injected material | Injection pressure (MPa) | Process-related apparent shear rate (s⁻¹) | Process-related apparent viscosity (Pa.s) |
|---|---|---|---|
| Pure UV-epoxy | 0.7 | 177 | 11.6±1.5 |
| | 4.2 | 879 | 10.9±1.6 |
| Nanocomposite-0.5wt% | 0.7 | 87 | 61.2±3.5 |
| | 4.2 | 554 | 41.3±4.4 |
| Nanocomposite-1wt% | 0.7 | 38 | 115.8±7.6 |
| | 4.2 | 414 | 49.1±5.2 |

on the viscosity of matrix and the aspect ratio (i.e., length/diameter) of the fillers, the extent of the shear forces to induce an orientation could be different [35]. In general, higher shear rates consequently causes the SWCNTs to align with the flow and frequently rotate by 180° in Jeffery orbits. The Brownian motion that may impose small disturbances contribute to the rotational motion by increasing the frequency of Jeffery orbits [36]. Therefore, higher $\dot{\gamma}_{app}$ corresponding to the high micro-injection pressure (i.e., $P_2$) is expected to increase the degree of orientation of nanotubes.

4.3. Morphological characterization of the 3D-reinforced beams

The fracture surface of a few representative 3D-reinforced (resin- and NC-injected) beams in tensile testing was observed under SEM in order to examine the matrix-fiber interface. Figure 8a shows a SEM image of typical fracture surface of a resin-injected beam prepared at 0.7 MPa and Figure 8b is close-up view of the surface of a microfiber. No perpendicular microfibers (i.e., microfibers in transverse layers) are seen and the fracture surface is extensively embedded with the surrounding matrix. This suggests that the cohesive failure took place in the region filled with the surrounding resin. Similar failure mechanism was observed for the fracture surface of the nanocomposite-injected beams. In addition, no debonding and no pull-out of the embedded microfibers are observed, indicating that the microfibers were strongly bonded to the surrounding matrix. This confirms that the very low shrinkage of the UV-epoxy used in this study prevented the

17

probable shrinkage-induced detachment of the microfiber surface from the microfluidic channel walls.

Figures 8c and 8d show TEM images of the nanocomposite (0.5wt% SWCNTs) microfibers (i.e., the nanocomposite filled the microfluidic channels) along the longitudinal direction for the nanocomposite injected beams prepared at the low and high injection pressures, respectively. Figure 8e and 8f show TEM images of the nanocomposite containing 1wt% for similar processing conditions. The arrows show the direction of flow inside the microfluidic channels along the longitudinal direction of the beams. For the beams prepared at low injection pressure (i.e., corresponding to the low shear rate), the TEM image of embedded microfiber (Figure 8c and 8e) do not indicate any preferential orientation and the nanotube aggregates are randomly oriented in the matrix. A clear change in the orientation of SWCNTs in the microfibers along the longitudinal direction is observed for the microfluidic channels filled at high injection pressure (i.e., corresponding to the higher shear rate) (Figure 8d and 8f). The higher pressure induced shear rate caused the nanotube aggregates to be aligned in the longitudinal channels along the direction of flow. Considering the fact that the nanotubes typically tend to exist as entangled agglomerates when mixed into a polymer matrix, some nanotubes remain randomly oriented in their aggregates. However, most of nanotube aggregates were well stretched along their lengths. Although the degree of orientation increased with the increase of shear rate by applying higher micro-injection pressure, it is still far from a perfect alignment. Comparing the TEM images for two different injection pressures suggests that higher shear rate not only contributes to the CNTs alignment but also enables their further dispersion within the matrix. Note that no preferential orientation of SWCNTs aggregates was observed in the microfluidic channels along the width direction of 3D-reinforced beam for both micro-injection cases.
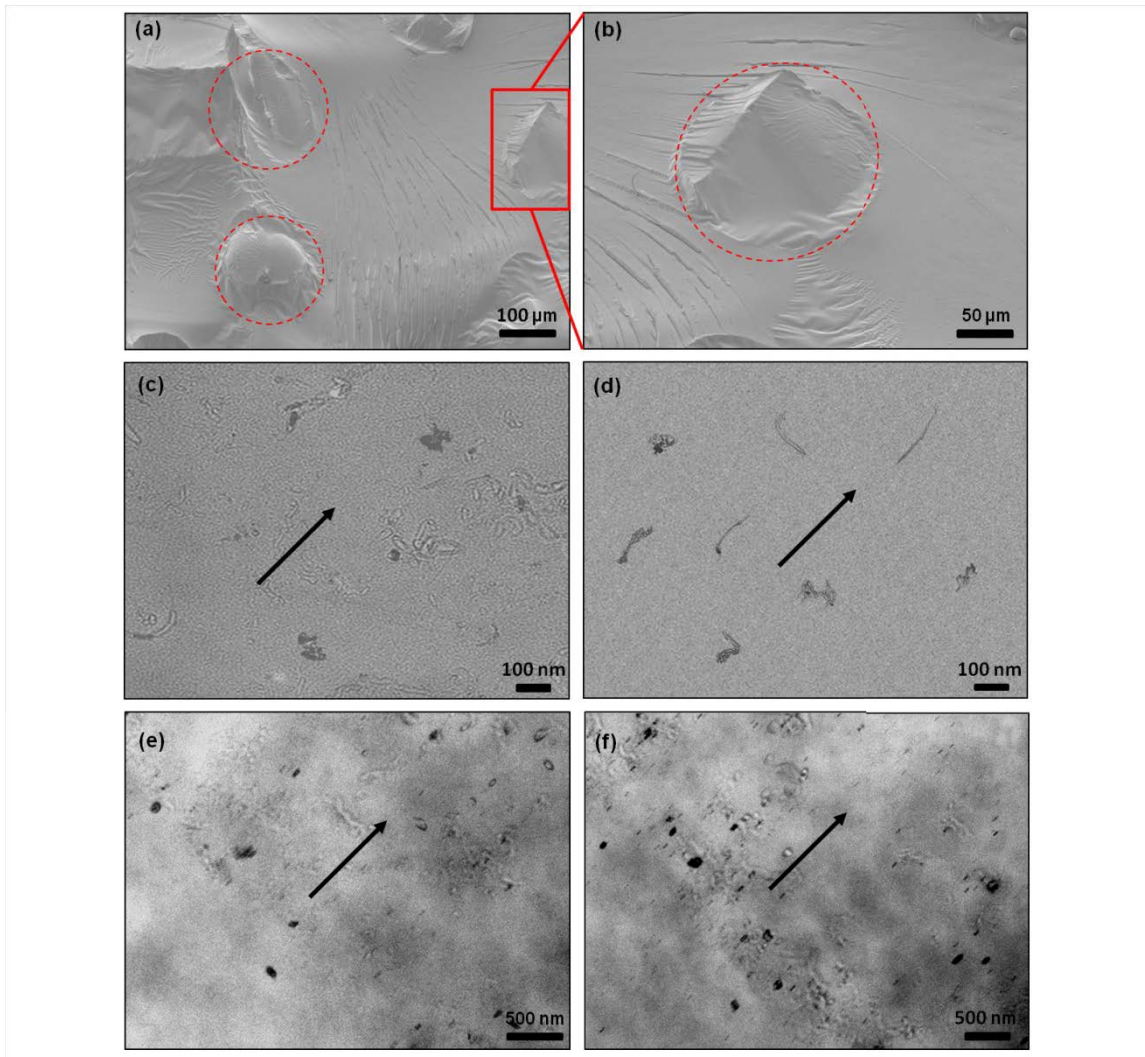
18

Figure 8. SEM images of typical fracture surface of (a) a representative injected beam filled at 0.7 MPa and (b) a close-up view of an embedded microfiber. The red-pointed circles highlight the microfibers; and TEM images of SWCNT orientation state inside the microchannels along the longitudinal direction for the nanocomposite (0.5wt%) injected beams filled at (c) low injection pressure and (d) high injection pressure and for the nanocomposite (1wt%) injected filled at (e) low injection pressure and (f) high injection pressure (arrows show the direction of flow in longitudinal direction of the beam).

## 4.4. Mechanical properties

The influence of CNTs and their orientation on the 3D-reinforced beams mechanical properties was studied under tensile loading. Figure 9 shows stress-strain curves of the pure resin and nanocomposite injected beams for the low and the high injection pressures. The error bars were calculated from the 95% confidence intervals on the mean value

obtained from the measurement. The stress-strain curves of the resin and NC-injected beams show a linear behavior followed by a short plastic response of the stress under strain before failure. This is a typical behavior of brittle polymers like epoxies. The failure behavior of the 3D-reinforced beams were slightly influenced by the addition of the SWCNTs, estimated to be ~0.18wt% (0.5wt% in nanocomposite microfibers) and ~0.35wt% (1wt% in nanocomposite microfibers) in the overall beam volume. Table 3 summarize the mechanical properties of the 3D-reinforced beams, the bulk epoxies and their deviations. The Young's modulus and the tensile strength of the resin-injected beams were measured to be 2.34 GPa and 64.7 MPa, respectively. For the NC-injected beams containing 0.18wt% of nanotubes, prepared at low injection pressure, average Young's modulus increased to 2.51 GPa, about a 7% enhancement. Their failure strengths increased by 6% to a value of 68.6 MPa. The incorporation of 0.35wt% SWCNTs further increased the Young's modulus (by 14%) and the tensile strength (by 13%) of the 3D-reinforced beams. A fairly good dispersion of SWCNTs within the UV-epoxy matrix and also a proper stress transfer between the host polymer matrix (the epoxy) and the carbon nanotubes are believed to be responsible for the reasonable increase in the NC-injected beams mechanical properties (stiffness and strength). The interfacial bonding between SWCNTs and epoxy molecules through the functional groups are thought to facilitate load transfer. Figure 10 represents two proposed interaction mechanisms in this study. Covalent grafting of carboxylic groups at the nanotube surfaces offers interaction possibility with the epoxy groups [37]. Non-covalent functionalization of SWCNTs using ZnPP affords the opportunity for additional interaction with epoxy matrix [10]. The ZnPP molecules can interact with the epoxy molecules through their carboxylic groups. The functional groups provided by both covalent and non-covalent functionalizations of the SWCNTs are capable to interact with epoxy groups, potentially leading to an enhanced stress transfer.

The higher micro-injection pressure led to further improvement in mechanical properties of the 3D-reinforced beams for the same nanotube loading. The average Young's modulus increased by 13% for 3D-reinforced beams containing 0.18wt% nanotubes and 25% for the beams with 0.35wt% nanotubes compared to the resin-injected beams. For both nanotube loadings, average beams Young's modulus improvements
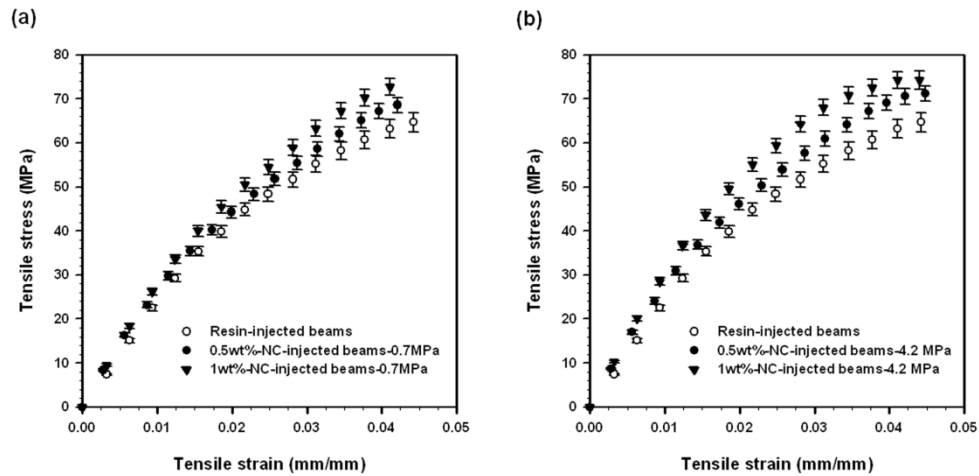
20

Figure 9. Tensile properties of the 3D reinforced beams: Averaged stress-strain curves of the resin and NG injected beams filled (a) at 0.7 MPa and (b) 4.2 MPa injection pressure.

were doubled when compared to the beams prepared at low injection pressure. These considerable improvements (above average compared to those reported in literature as listed in Table 4) in mechanical properties could be attributed to SWCNTs shear-induced orientation. Another contribution may come from probable better dispersion caused by breakage of aggregates at higher shear [10]. Given the amount of SWCNTs added, the considerable beams Young's modulus improvement, when compared to the bulk-nanocomposite (i.e., molded sample) and also with those reported in literature (Table 4), suggests the effectiveness of the present manufacturing method to take the advantage of nanotube orientation in microfluidic network.

Table 3. Mechanical properties of the resin-injected and the nanocomposite-injected beams prepared by micro-injection of the materials at two different shear rates and bulk epoxies.

21

| Type of beams | Young's Modulus (GPa) | Young's Modulus Var. (%) | Tensile Strength (MPa) | Tensile Strength Var. (%) | Elongation at break (%) | Elongation at break Var. (%) |
|---|---|---|---|---|---|---|
| Bulk UV-epoxy | 1.32±0.02 | --- | 50.4±1.1 | --- | 14.6±0.4 | --- |
| Bulk-EPON862 | 3.10±0.05 | --- | 79.8±1.6 | --- | 3.2±0.1 | --- |
| Resin-injected | 2.34±0.03 | 0 | 64.7±0.7 | 0 | 4.4±0.1 | 0 |
| 0.5wt%-NC-injected-0.7 MPa | 2.51±0.05 | +7 | 68.6±1.4 | +6 | 4.2±0.2 | -4 |
| 1wt%-NC-injected-0.7 MPa | 2.67±0.03 | +14 | 72.7±2.1 | +13 | 4.1±0.1 | -7 |
| 0.5wt%-NC-injected-4.2 MPa | 2.65±0.04 | +13 | 71.1±1.4 | +10 | 4.5±0.1 | +2 |
| 1wt%-NC-injected-4.2 MPa | 2.93±0.07 | +25 | 74.3±1.8 | +15 | 4.4±0.1 | 0 |

Figure 10. Schematic of proposed interaction mechanisms between SWCNTs and epoxy through both carboxylic group grafting [31] and non-covalent functionalization of SWCNTs [9].

4.5. Stiffness prediction with homogenization model

Table 5 lists the computed Young's modulus of the resin- and nanocomposite-coated microfibers for aligned, partially aligned and randomly oriented cases. The predictions of the Young's modulus of the UV-epoxy microfibers increased by about 70% following the addition of 1 wt% of randomly oriented CNTs while this value for the aligned CNTs showed an increase of 405% in comparison with UV-epoxy fibers. Table 6 lists the final analytical predictions of the resin and NC-injected beams for the different cases studied. The NC-injected beams with the CNTs alignment along the longitudinal direction and random

orientation in transverse direction showed the highest value of the Young's modulus. Although the stiffness of a layer in longitudinal direction increases with the nanotube alignment in the channels, this factor decreases the longitudinal stiffness in transverse layers. In the resin-injected beams, there are only small differences between the analytical and experimental results (4%). This confirms that the microfibers are strongly bonded to the surrounding matrix, as observed by SEM. Assuming that there is the same initial difference between the analytical and experimental estimations for the NG-injected beams as for the resin-injected beams, the 50% aligned CNTs in the longitudinal and randomly oriented in the transverse layers appears to be the most appropriate assumption the structural state of CNTs in NG-injected beams prepared at high injection pressure. This is also supported by TEM observations. On the other hand, applying the same reasoning to keep the initial difference between the analytical and experimental estimations the NG injected beams and the resin injected beams under low pressure supports TEM observations: low injection pressure results in randomly oriented CNTs in both longitudinal and transverse layers.

The reasonable consistency between the analytical estimations and the tensile experiments indicates that the CNTs reinforcement is not far from achieving its theoretical potential. The differences might be attributed to the following phenomena: probable The presence of impurities produced along with CNTs like amorphous carbon which was not

Table 4. Comparison of increase of storage modulus at 25°C by adding SWCNTs to epoxy matrices achieved in our work with those reported in literature.

| Researcher | | SWCNTs wt.% | Increase of property (%) | Normalized (Increase of property/wt.%) (%) |
|---|---|---|---|---|
| Barrera et al. [7] | | 1.0 | 31 | 31 |
| Sun et al. [12] | | 1.0 | 26 | 26 |
| Wang et al. [8] | | 0.5 | 30 | 60 |
| Our results | 0.5wt% – 0.7 MPa | 0.18 (whole beam) | 7 | 39 |
| | 1wt% – 0.7 MPa | 0.33 (whole beam) | 14 | 42 |
| | 0.5wt% – 4.2 MPa | 0.18 (whole beam) | 13 | 72 |
| | 1wt% – 4.2 MPa | 0.33 (whole beam) | 25 | 75 |
| | Bulk-epoxy nanocomposite | 0.3 (molded) | 10 | 33 |

Table 5. Analytical Young's modulus of the resin and NG based microfibers with aligned, partially aligned and randomly oriented CNTs.

| Type of microfiber | Young's modulus (GPa) | | Young's modulus Var.(%) | |
|---|---|---|---|---|
| Non-reinforced | 1.32 | | 0 | |
| | V.F. 0.5% | V.F. 1% | V.F. 0.5% | V.F. 1% |
| Random oriented CNTs | 1.78 | 2.24 | 35% | 70% |
| Partially aligned CNTs (20%) | 2.25 | 3.26 | 79% | 147% |
| Partially aligned CNTs (50%) | 3.35 | 5.36 | 153% | 306% |
| Aligned CNTs | 4 | 6.67 | 203% | 405% |

considered in modeling, may affect the mechanical properties. The curvature of the flexible CNTs bundles may reduce their effective aspect ratio as observed in TEM images [38]. In addition, the slippage of the inner nanotubes in bundles may also decrease the effectiveness of nanoreinforcements. A homogeneous orientation state was assumed in whole cross section area of the microfluidic channels. However, the shear rate maximum at the channel wall gradually reduces towards the channel center at which the shear rate becomes zero. In other words, the carbon nanotubes near the microfluidic channel center were subjected to very low shear rates and consequently might be randomly bond. This effect could be reduced through the injection of even small microchannels. The Mori-Tanaka model has an intrinsic accuracy, for the volume fraction considered, it should be quite good.

Table 6. Analytical and experimental Young's modulus of the resin and NG injected beams with aligned, partially aligned and randomly oriented CNTs.

| CNTs orientation state in | | Longitudinal Young's modulus (GPa) | | | | | |
|---|---|---|---|---|---|---|---|
| | | Experimental Injection pressure | | | | Analytical | |
| Longitudinal Fibers | Transverse Fibers | 0.7 MPa | | 4.2 MPa | | V.F. 0.5% | V.F. 1% |
| | | V.F. 0.5% | V.F. 1% | V.F. 0.5% | V.F. 1% | | |
| Resin injected beams | | 2.34±0.03 | | | | 2.4 | |
| Aligned | Aligned | | | | | 2.97 | 3.54 |
| Partially Aligned | Partially Aligned | | | | | 2.62 | 2.89 |
| Random | Random | 2.51±0.05 | 2.67±0.03 | | | 2.59 | 2.78 |
| Aligned | Random | | | | | 3.01 | 3.62 |
| Aligned | Partially Aligned | | | | | 2.95 | 3.5 |
| Partially Aligned (20%) | Random | | | | | 2.69 | 2.96 |
| Partially Aligned (50%) | Random | | | 2.65±0.04 | 2.93±0.07 | 2.89 | 3.37 |

## 5. Conclusion

Three dimensional microstructured beams reinforced with SWCNT/epoxy nanocomposite with spatial localization and orientation of the nanotubes were fabricated via the nanocomposite micro injection of a microfluidic network. The nanotube orientation was performed by taking the advantages of shear flow and dimensional constraining of small diameter channels. The SEM observations revealed a fair dispersion of SWCNTs aggregates in UV epoxy matrix after the ultrasonication and three roll mill mixing. The morphological analysis using TEM showed a random orientation of SWCNT aggregate at the lower shear rate, caused by the lower injection pressure, while the nanotubes were partially aligned along the direction of flow at higher shear rate, caused by the higher injection pressure. For the beams reinforced with the partially aligned nanotube aggregates, the improvement of Young's modulus was doubled compared to the beams with randomly oriented nanotubes. The stiffness values of the beams predicted by the micromechanical

model for the case of partial orientation of nanotubes were close to the experimental data, indicating the efficiency of the present manufacturing method in orientation and localization of CNTs within a polymer matrix. To further align the nanotubes, higher injection pressures (i.e., higher shear rate) and smaller diameter microfluidic channels (i.e., higher constraining effect) could be employed. The flexibility of this manufacturing method enables the design of functional 3D reinforced nanocomposite macroscopic products for a wide variety of applications such as structural composite applications and components for micro electromechanical systems. It is worth noting that the nanomaterials incorporated inside the 3D microfluidic network can be used to enhance the structure properties other than mechanical such as electrical or thermal conductivity.

Acknowledgments

Appendix A

"The components of Eshelby tensor for a fibrous reinforcement are [27]:

$$S_{2222} = \frac{1}{2(1-Q_m)}\left(1-2\nu_m+\frac{3a^2-1}{a^2-1}-\left(1-2\nu_m+\frac{3a^2}{a^2-1}\right)g\right),$$

$$S_{1111} = S_{3333} = \frac{3}{8(1-\nu_m)}\frac{a^2}{a^2-1}+\frac{1}{4(1-Q_m)}\left(1-2\nu_m-\frac{9}{4(a^2-1)}\right)g,$$

$$S_{133} = S_{3311} = -\frac{1}{4(1-Q_m)}\frac{a^2}{2(a^2-1)}(1-2Q_m - \frac{3}{4(a^2-1)})g$$

$$S_{122} = S_{3322} = \frac{1}{2(1-\nu_m)}\frac{a^2}{a^2-1} - \frac{1}{4(1-Q_m)}(\frac{3a^2}{(a^2-1)}-(1-2Q_m))g,$$

$$S_{2211} = S_{2233} = -\frac{1}{2(1-\nu_m)}(1-2\nu_m + \frac{1}{a^2-1}) - \frac{1}{2(1-Q_m)}(\frac{3}{2(a^2-1)}-1-2Q_m)g,$$

$$S_{3131} = \frac{1}{4(1-Q_m)}(\frac{a^2}{2(a^2-1)}) + (\frac{3}{4(a^2-1)}-1-2Q_m)g,$$

$$S_{212} = S_{3232} = \frac{1}{4(1-Q_m)}(1-2\nu_m - \frac{a^2+1}{2(a^2-1)}) - \frac{1}{2}(\frac{3(a^2+1)}{4(a^2-1)}-1-2Q_m)g,$$

where $a$ is the aspect ratio of the reinforcement defined as the ratio of its length to its diameter and $g$ for fiber reinforcement is given by:

$$g = \frac{a}{(a^2-1)^{3/2}}[a(a^2-1)^{1/2} - \cosh^{-1}a],$$

Then, the Eshelby tensor, $S$, has the following matrix form:

$$S = \begin{pmatrix} S_{1111} & S_{1122} & S_{1133} & 0 & 0 & 0 \\ S_{2211} & S_{2222} & S_{22333} & 0 & 0 & 0 \\ S_{3311} & S_{3322} & S_{3333} & 0 & 0 & 0 \\ 0 & 0 & 0 & 2S_{3232} & 0 & 0 \\ 0 & 0 & 0 & 0 & 2S_{3131} & 0 \\ 0 & 0 & 0 & 0 & 0 & 2S_{1212} \end{pmatrix}$$

References

1. Ear Y and Silverman E. MRS Bulletin 2007;32(4):328-334.
2. Mirfakhrai T, KrishnaPrasad R, Nojeh A, and Madden JDW. Nanotechnology 2008;19(31):315706, 1-8.

3.  Sahoo NG, Jung YC, Yoo HJ, and Cho JW. Composites Science and Technology 2007;67(9):1920-1929.

4.  Varadan VK, Varadan VV, and Motojima S. Three-dimensional polymeric and ceramic MEMS and their applications. Smart Structures and Materials 1996: Smart Electronics and MEMS. San Diego, CA, 1996.

5.  Varadan VK, Xie, J., Ji, T. BioMEMS and Smart Nanostructures, Proceedings of SPIE 2001;4590:134-141.

6.  Coleman JN, Khan U, and Gun'ko YK. Advanced Materials 2006;18(6):689-706.

7.  Barrera EV, Zhu J, Peng HQ, Rodriguez-Macias F, Margrave JL, Khabashesku VN, Imam AM, and Lozano K. Advanced Functional Materials 2004;14(7):643-648.

8.  Wang S, Liang R, Wang B, and Zhang C. Nanotechnology 2008;19(8):085710,-7.

9.  Wang SR, Liang ZY, Liu T, Wang B, and Zhang C. Nanotechnology 2006;17(6):1551-1557.

10. Lebel LL, Aissa B, El Khakani MA, and Therriault D. Composites Science and Technology 2010;70(3):518-524.

11. Nakashima N and Fujigaya T. Chemistry Letters 2007;36(6):692-697.

12. Sun L, Warren GL, O'Reilly JY, Everett WN, Lee SM, Davis D, Lagoudas D, and Sue HJ. Carbon 2008;46(2):320-328.

13. Zhu J, Kim JD, Peng HQ, Margrave JL, Khabashesku VN, and Barrera EV. Nano Letters 2003;3(8):1107-1113.

14. Fan ZH and Advani SG. Polymer 2005;46(14):5232-5240.

15. Abbasi S, Carreau PJ, and Derdouri A. Polymer 2010;51(4):922-935.

16. Kimura T, Ago H, Tobita M, Ohshima S, Kyotani M, and Yumura M. Advanced Materials 2002;14(19):1380-1383.

17. Chronakis IS. Journal of Materials Processing Technology 2005;167(2-3):283-293.

18. Zhou W, Vavro J, Guthy C, Winey KI, Fischer JE, Ericson LM, Ramesh S, Saini R, Davis VA, Kittrell C, Pasquali M, Hauge RH, and Smalley RE. Journal of Applied Physics 2004;95(2):649-655.

19. Sandler JKW, Pegel S, Cadek M, Gojny F, van Es M, Lohmar J, Blau WJ, Schulte K, Windle AH, and Shaffer MSP. Polymer 2004;45(6):2001-2015.

20. Lebel LL, Aissa B, Paez OA, El Khakani MA, and Therriault D. Journal of Micromechanics and Microengineering 2009;19(12):125009,-7.

21. Braidy N, El Khakani MA, and Botton GA. Chemical Physics Letters 2002;354(1-2):88-92.

22. Therriault D, Shepherd RF, White SR, and Lewis JA. Advanced Materials 2005;17(4):395-399.

23. Therriault D, White SR, and Lewis JA. Nature Materials 2003;2(4):265-271.

24. Bruneaux J, Therriault D, and Heuzey MC. Journal of Micromechanics and Microengineering 2008;18(11):115020,-11.

25. Mori T, Tanaka K. Acta metallurgica 1973;21:571-574.

26. Eshelby JD. Proceedings of the Royal Society of London A 1957;241(1226):376-396.

27. Schjodt-Thomsen J and Pyrz R. Mechanics of Materials 2001;33(10):531-544.

28. Maekawa Z, Hamada H, and Yokoyama A. Composite Structures 5 1989:701-714.

29. Wang LF and Zheng QS. Applied Physics Letters 2007;90(15):153113,1-3.

30. Bandow S, Asaka S, Saito Y, Rao AM, Grigorian L, Richter E, and Eklund PC. Physical Review Letters 1998;80(17):3779-3782.

31. Baker SE, Cai W, Lasseter TL, Weidkamp KP, and Hamers RJ. Nano Letters 2002;2(12):1413-1417.

32. Okpalugo TIT, Papakonstantinou P, Murphy H, McLaughlin J, and Brown NMD. Carbon 2005;43(1):153-161.

33. Gojny FH, Wichmann MHG, Fiedler B, and Schulte K. Composites Science and Technology 2005;65(15-16):2300-2313.

34. Thostenson ET and Chou TW. Carbon 2006;44(14):3022-3029.

35. Hobbie EK, Wang H, Kim H, Lin-Gibson S, and Grulke EA. Physics of Fluids 2003;15(5):1196-1202.

36. Hogberg SM and Lundstrom TS. Plastics Rubber and Composites 2011;40(2):70-7.

37. Moniruzzaman M, Du FM, Romero N, and Winey KI. Polymer 2006;47(1):293-298.

38. Li XD, Gao HS, Scrivens WA, Fei DL, Xu XY, Sutton MA, Reynolds AP, and Myrick ML. Journal of Nanoscience and Nanotechnology 2007;7(7):2309-2317.